Applied Physics A (2022) 128:4
https://doi.org/10.1007/s00339-021-05128-x

Applied Physics A
Materials Science & Processing

High lithium-ion conductivity in all-solid-state lithium batteries by Sb doping LLZO

Xinghua Liang[1] · Suo Li[1] · Guanhua Yang[1,3] · Xi Wu[2] · Dongxue Huang[1] · Yujue Ning[1] · JianGuo Luo[1] · Zhijie Fang[1]

Received: 5 August 2021 / Accepted: 20 November 2021 / Published online: 4 December 2021

Abstract

All-solid-state lithium batteries are considered to be the most promising electrochemical energy storage equipment due to their high safety, high energy density, and simple structure. However, the preparation of solid electrolytes with high lithium-ion conductivity and superior electrode–electrolyte interface contact is the development needs. In this study, the electronic structures of garnet-type $Li_7La_3Zr_2O_{12}$ (LLZO) and Sb-doped LLZO electrolytes were investigated using the first-principles method based on density functional theory (DFT). Theoretical calculations have confirmed that elemental doping facilitates the migration of lithium ions in solid-state electrolytes at the micro-atomic level. Based on the theoretical calculations and analysis results, $Li_{6.7}La_3Zr_{1.7}Sb_{0.3}O_{12}$ (LLZSbO) with high ionic conductivity was synthesized by the conventional solid-state method. To reduce the interfacial impedance between electrolyte and electrode, the composite solid electrolytes (CSEs) containing LLZSbO active fillers were prepared by the solution casting method. The prepared CSEs exhibits a high ionic conductivity of 0.97×10^{-4} S cm^{-1} at 30 °C and a stable electrochemical window of 5.3 V as well as the lithium-ion transference number up to 0.37. The all-solid-state battery using the CSEs prepared with 20 wt% LLZSbO has excellent rate performance and cycle stability. The initial discharge specific capacity can reach 148.4 mAh g^{-1} when the rate is 0.1 C. The capacity can cover 138.8 mAh g^{-1} after 100 cycles at 0.2 C with a capacity retention rate of 97.5%.

Keywords Solid electrolyte · $Li_7La_3Zr_2O_{12}$ · First principles · Ionic conductivity · All-solid-state lithium battery

1 Introduction

In recent years, lithium-ion batteries have been widely used in transportation, electronic equipment and other fields due to the advantages of high energy density, low self-discharge and lightweight [1–3]. However, the preparation of solid electrolytes with high lithium-ion conductivity and superior electrode–electrolyte interface contact is an urgent need for development. In order to solve the safety risks of liquid electrolytes in lithium-ion batteries fundamentally, the structural design of using solid electrolytes replacing flammable and explosive liquid electrolytes for assembling all-solid-state lithium batteries (ASSLiBs) is proposed [4–6]. As an important part of SSLiBs, the performance of solid electrolytes directly affects the electrochemical performance of ASSLiBs, so the majority of researchers have conducted extensive research on solid electrolytes [7, 8].

Polyethylene oxide (PEO), as solid polymer electrolytes (SPEs), is the closest class of solid electrolyte to commercial production applications due to its good film-forming properties and good contact between electrode and electrolyte interface [9–11]. However, the PEO has high crystallinity and the movement of Li^+ on the chain segment is hindered at room temperature, resulting in ionic conductivity of only 10^{-6}–10^{-8} S cm^{-1} [12–14]. To enhance its electrochemical properties, the PEO matrix is usually refined by adding inorganic fillers or plasticizers, blending with polymers [15, 16]. Recently, the composite solid electrolytes (CSEs) prepared by combining PEO matrix with inorganic fillers have excellent electrochemical properties, this is due to the CSEs consisting of polymer matrixes and active or inert ceramic

✉ Guanhua Yang
yghchem@163.com

[1] Guangxi Key Laboratory of Automobile Components and Vehicle Technology, Guangxi University of Science and Technology, Liuzhou 545006, People's Republic of China

[2] School of Materials and Energy, Guangdong University of Technology, Guangzhou 510006, China

[3] Guangxi Key Laboratory of Low Carbon Energy Material, Guangxi Normal University, Guilin 541004, China

particles/nanowires combine the excellent flexibility of polymer electrolytes with the high ionic conductivity of inorganic electrolytes [17–19]. Wimalaweera et al. [20] added inert inorganic fillers Al_2O_3 to the PEO-$LiClO_4$ matrix and the prepared CSEs had an ionic conductivity of 10^{-5} S cm^{-1} at room temperature. The addition of inert inorganic fillers destroys the regularity of the molecular chain arrangement of SPEs, so the reduction of crystallinity is beneficial to the result of Li^+ migration. Researchers believe that adding active inorganic ceramic fillers with ion conductivity to the polymer matrix for preparing CSEs has great advantages in improving ion conductivity [21–23].

Compared with other inorganic ceramic electrolytes, the garnet-type $Li_7La_3Zr_2O_{12}$ (LLZO) has the advantages of a wide electrochemical window (> 5 V) and metal lithium contact stability, which have attracted widespread attention. Nevertheless, owing to the different conditions (synthesis method, sintering temperature, etc.) for the preparation of LLZO, two crystal structures are obtained: cubic phase and tetragonal phase. The ionic conductivity of the cubic phase is two orders of magnitude higher than that of the tetragonal phase [24, 25]. For preparing LLZO with a cubic phase structure and high ionic conductivity, the doping of Ta, Nb, Sb, Al, Ga, and other elements in Zr sites and Li sites is a good strategy, which can increase lithium ion vacancy concentration and improve lithium ion transport channels and stabilize LLZO cubic structure [26, 27]. Although doping of Al^{3+} [28], Ga^{3+} [29] elements at the Li site can form lithium ion vacancies, the doped elements occupy lithium ion sites and can hinder the transport of lithium ions. In contrast, doping elements such as Sb^{5+} at Zr sites can increase lithium ion vacancies, improve lithium ion occupancy, and greatly improve ionic conductivity. Therefore, we choose to dope the high-valence element Sb^{5+} at the Zr site to introduce a higher concentration of lithium vacancies in the crystal, thus further increasing the mobility of lithium ions [30, 31].

Moreover, through first-principles modeling and simulation based on quantum mechanics can understand the electrochemical stability mechanism of electrolytes from the atomic point of view and provide theoretically effective tools for elemental doping of garnet-type electrolytes [32, 33]. KC et al. [34] studied Li^+ defects in LLZO by density functional theory based on first principles. The results show that Li^+ vacancy defects are better than interstitial Li^+ defects in thermodynamics, so Li^+ is more inclined to vacancy migration in the structure. MIARA et al. [35] mixed Rb and Ta into the LLZO to construct LLRbZO and LLTaZO models respectively and performed simulation analysis. The research results show that Ta doping will significantly improve the ionic conductivity of LLZO, which provides theoretical support for the experimental preparation. Theoretical analysis based on first principles understands that elemental doping is an effective measure to promote the conductivity of electrolyte ions and is critical for the improvement of the electrochemical properties of CSE. Here we propose, design of Sb-doped LLZO electrolytes based on first-principles calculations for the preparation of CSEs applied to ASSLiBs provides theoretical support for improving the electrochemical performance of ASSLiBs. To develop CSEs with high ionic conductivity, Yang et al. [36] added LLZO, Al-LLZO and Ta-LLZO prepared by electrostatic spinning method to PAN-$LiClO_4$ matrix, respectively. The ionic conductivity of all the prepared CSEs could reach 10^{-4} S cm^{-1}. Li et al. [37] have prepared CSEs by adding Ga-doped LLZO to the PEO matrix with a maximum ionic conductivity of 7.2×10^{-5} S cm^{-1} at room temperature. Ma et al. [38] have studied CSEs consisting of a PEO matrix with Si-doped LLZO, which exhibited an ionic conductivity of 2.24×10^{-4} S cm^{-1} at 50 °C. Cheng et al. [39] studied the conductivity of the CSEs prepared by adding $Li_{6.4}La_3Zr_{1.4}Ta_{0.6}O_{12}$ to the PEO-$LiClO_4$ matrix through the solution casting method. It is reported that the prepared CSEs have a high ionic conductivity of 4.8×10^{-4} S cm^{-1} at 60 °C. The ASSLiBs assembled with the CSEs can still reach 140 mAh g^{-1} of specific capacity even after 500 cycles at a rate of 1 C. Song et al. [40] studied the effect of adding small particle size inorganic fillers on the electrochemical performance of CSEs. The CSEs prepared by mixing 15 wt% of nanoscale $Li_{6.5}La_3Zr_{1.75}Nb_{0.25}O_{12}$ and PEO by ball milling exhibit a high ionic conductivity of 3.6×10^{-4} S cm^{-1} at 30 °C. However, most of the studies on CSEs have focused on improving the electrochemical performance of CSEs from elemental doping, particle size or filler concentration of inorganic oxide electrolytes. In this paper, elemental doping, particle size, and filler concentration are considered together to prepare CSEs by preparing inorganic fillers with small particle sizes. And we select the appropriate LLZSbO concentration to provide advantages for improving the electrochemical performance of CSEs.

Herein, we report the electronic structure of Sb-doped LLZO electrolyte was studied by the first-principles method based on DFT. The crystal structure of LLZO was designed according to the results of theoretical calculation and analysis. The $Li_{7-x}La_3Zr_{2-x}Sb_xO_{12}$ ($x = 0$–0.4) was synthesized by solid-state method. Subsequently, the solution casting method was used to prepare CSEs containing LLZSbO active fillers. The results show that the flexible CSEs prepared with 20 wt% LLZSbO show excellent electrochemical performance and the assembled solid-state battery also shows excellent cycle and rate performance. This work aims to improve the electrochemical performance of all-solid-state lithium batteries and provide a possibility for subsequent improvements in the performance of ASSLiBs.

2 Experimental section

2.1 Computational methodology

The CASTEP module in Materials Studio (MS) was used to calculate the interaction potential between ions and electrons. The Perdew–Burke–Enzerhof (PBE) exchange-correlation functional based on density functional theory (DFT) was used theoretical calculations [41]. In this study, the calculation accuracy is fine, and the valence electrons selected for atomic pseudopotence calculation are Li $1s^2$ $2s^1$, O $2s^2$ $2p^4$, Zr $4s^2$ $4p^6$ $4d^2$ $5s^2$, La $5s^2$ $5p^6$ $5d^1$ $6s^2$, Sb $4d^{10}$ $5s^2$ $5p^3$. The truncation energy is 600 eV, and the integration of the Brillouin region is calculated using a $4 \times 4 \times 4$ Monkhorst–Pack k-point grid for iteration.

The cubic LLZO (CC: 422,259) structure was created based on the International Crystal Structure Database (ICSD). Its space group is *Ia3d*, and the cell parameters are $a = b = c = 12.983$ Å. The crystal is connected by octahedral [ZrO_6] and dodecahedral [LaO_8] to form a skeleton structure, and Li ions are located at the position of 24d of tetrahedron and 96 h of dodecahedral, respectively. The model structure contains 256 ions and satisfies the stoichiometric formula $Li_{120}O_{96}Zr_{16}La_{24}$. In order to reduce the amount of calculation and calculation time, the supercell is changed into the primitive cell according to the principle of symmetry. The Zr position (3.25, 3.25, 3.25) is replaced by element Sb to generate the calculation model of doping: $Li_{60}O_{48}La_{12}Zr_8Sb_{48}$ (LLZO-Sb). The structure of the doped and undoped crystals was optimized. The optimized crystal structure is shown in Fig. S1(a, b).

2.2 Preparation of Sb doped $Li_{7-x}La_3Zr_{2-x}Sb_xO_{12}$ ($x = 0$–0.4)

The $Li_{7-x}La_3Zr_{2-x}Sb_xO_{12}$ ($x = 0$–0.4) samples were synthesized by conventional solid-state method. During the preparation process, $LiOH{\cdot}H_2O$ (Aladdin 98%), La_2O_3 (99.99%, Sinopharm Chemical Reagent Co., Ltd., China), ZrO_2 (Aladdin 99.99%) and Sb_2O_5 (Aladdin 99%) were mixed and ball-milled was conducted for 12 h [42]. The mixed raw materials were dried and sintered at 900 °C for 6 h to synthesize precursor powders. The got precursor powders were ball-milled for the second time in the same way to obtain the precursor samples with uniform particle size. After the precursor samples were dried, they were pressed into a circular block by cold isostatic pressing. The circular block was put into an alumina crucible containing the same precursor samples and sintered at 1100 °C for 10 h to synthesize $Li_{7-x}La_3Zr_{2-x}Sb_xO_{12}$ ($x = 0$–0.4).

2.3 Synthesis of CSEs

As shown in Fig. 1, the preparation of CSEs by the solution casting method: Before use, PEO (Sigma-Aldrich) and $LiClO_4$ (Sigma-Aldrich) respectively were vacuum-dried at 60 °C and 100 °C for 24 h. PEO and $LiClO_4$ were weighed according to the PEO: $LiClO_4$ molar ratio of 18:1 and dissolved in an appropriate amount of acetonitrile solution, then the solution was stirred at a constant temperature of 55 °C. After complete dissolution, inorganic fillers with different weight ratios (10–25 wt%) were added and stirred for 12 h to obtain a homogeneous solution, which was then poured on a polytetrafluoroethylene template and dried at 60 °C for 24 h.

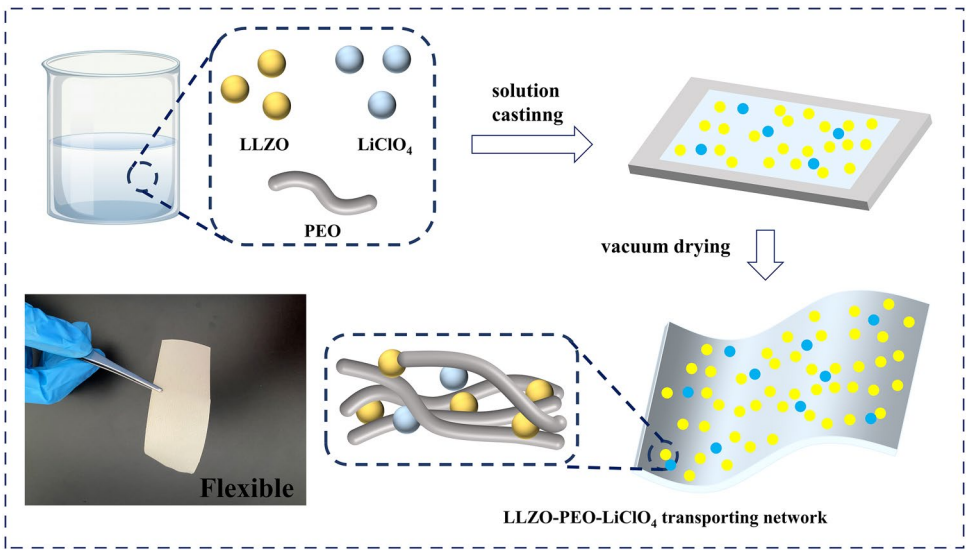

Fig. 1 Schematic pattern of the preparation process of the CSEs

2.4 Material characterization

The crystal structure of $Li_{7-x}La_3Zr_{2-x}Sb_xO_{12}$ ($x = 0$–0.4) powders and CSEs was characterized by X-ray diffraction (XRD, D8-Advance) with Cu-Kα as the radiation source and scanning angle from 10° to 80°. Scanning electron microscopy (SEM, ΣIGMA) was used to characterize the surface morphology of the samples. Thermal performance analysis of CSEs with different ceramic fillers by differential scanning calorimetry (DSC, DSC25 TA Instruments) at a temperature range of − 80–100 °C with the rising rate of 10 °C min^{-1}. AC impedance measurements were performed using an electrochemical workstation (DH7000, Jiangsu Donghua Analysis Instruments Co., Ltd) in the range of 0.01–1 MHz, and Eq. (1) is used to calculate the ionic conductivity:

$$\sigma = \frac{L}{R \cdot S} \tag{1}$$

Here, σ (S cm^{-1}) represents the ionic conductivity of the solid electrolyte, L (cm) represents the thickness of the solid electrolyte, R (Ω) represents the resistance measured by AC impedance and S (cm^2) represents the cross-sectional area of the solid electrolyte.

The lithium-ion transference number (t^+) of CSEs were fabricated into a blocking battery using double lithium sheets as symmetric electrodes under a 60 °C environment, and the DC polarization test and AC impedance test were performed under the condition of a polarization voltage of 10 mV and then calculated by Formula (2):

$$t^+ = \frac{I_{SS}(\Delta V - R_0 I_0)}{I_0(\Delta V - R_{SS} I_{SS})} \tag{2}$$

Here, I_0 (mA) and I_{SS} (mA) were the initial polarization current obtained from the DC polarization test and the steady-state polarization current, respectively. R_0 (Ω) and R_{SS} (Ω) were the pre-polarization resistance and post-polarization resistance, which obtained from the AC impedance test in the range of 0.01–1,000,000 Hz.

2.5 Preparation and electrochemical analysis of ASSLiBs

$LiFePO_4$ (LFP), polyvinylidene fluoride (PVDF), and conductive carbon black were used as raw materials for the preparation of cathode materials. According to the mass ratio of 8:1:1, the cathode was dissolved in N-methyl pyrrolidone (NMP) solvent. Then the obtained slurry was coated on the surface of aluminum foil and dried for 48 h at a vacuum temperature of 60 °C. The LFP/CSEs/Li batteries were assembled in an argon-filled glove box. The assembled coin cell was charged and discharged at different current densities in the voltage range of 2.8–4.0 V. Meanwhile, the AC impedance test was carried out in the frequency range of 0.01–100,000 Hz, and the AC amplitude was 5 mV.

3 Results and discussion

Figure 2a, b shows the partial state densities of elements near the Fermi surface. The peak strength and peak position in different regions are different, which is caused by the appearance of the electron orbital of Sb. The partial densities of states peaks at − 10 to − 4 eV and − 23–17 eV below the valence bands of the two crystal structures are due to the effect of the s, p orbitals of Li–O, La–O, and Zr-O. After doping, there is no effect on the peak position, and only the energy is slightly decreased, indicating that there is a strong covalent bond between Li 2 s, La 5 s, 5p, Zr 4p, and O 2 s, 2p. In the partial density map of LLZO-Sb, a new peak position is added at the low energy level − 31.5 eV, and the peak value is 19.4 eV. The resulting peak position is the function of the Sb d orbital. It is precisely the function of the d orbital of Sb that the electronic structure of LLZO-Sb changes fundamentally, which affects the electrochemical performance of LLZO.

The distribution of electrons in each atomic orbit is different and the bonding of atoms in the molecule can be understood through overlap population analysis. The atom overlap population calculation results are shown in Table 1 that the number of electrons in the s and d orbitals of Li, Zr, and La decrease after Sb doped, but the number of net charges of Li, Zr, and La increase, indicating that the degree of Li ionization grew and thus more Li^+ can transfer freely in the structure. The increase in La and Zr in the net charge number reflects that the interaction with O^{2-} is enhanced and improves the stability of the structure. Meanwhile, Sb occupies part of the electrons of O to form Sb-O bonds, resulting in reducing the charge of O. Due to the formation of Sb-O bonds has greater binding energy than doping other elements [43, 44]. The binding energy of the electrolyte LLZO is larger, the more stable the crystal structure [45]. Therefore, Sb-doped LLZO is beneficial to improve the stability of the structure. In Table S1, the decrease in the overlap population number of Li–O after doping indicates that the covalency between Li–O is weakened and therefore the mobility ability of Li^+ is improved. In addition, the improvement in the O-La population number after doping suggests that the covalency between O-La is enhanced, which enhances the stability of the structure.

The ease of Li^+ transference in the electrolyte material directly determines its electrical conductivity. If Li^+ has a smaller energy barrier in the electrolyte, the Li^+ migration rate can be increased, thereby improving conductivity [46, 47]. $DMol^3$ is used to study the energy barrier of Li^+

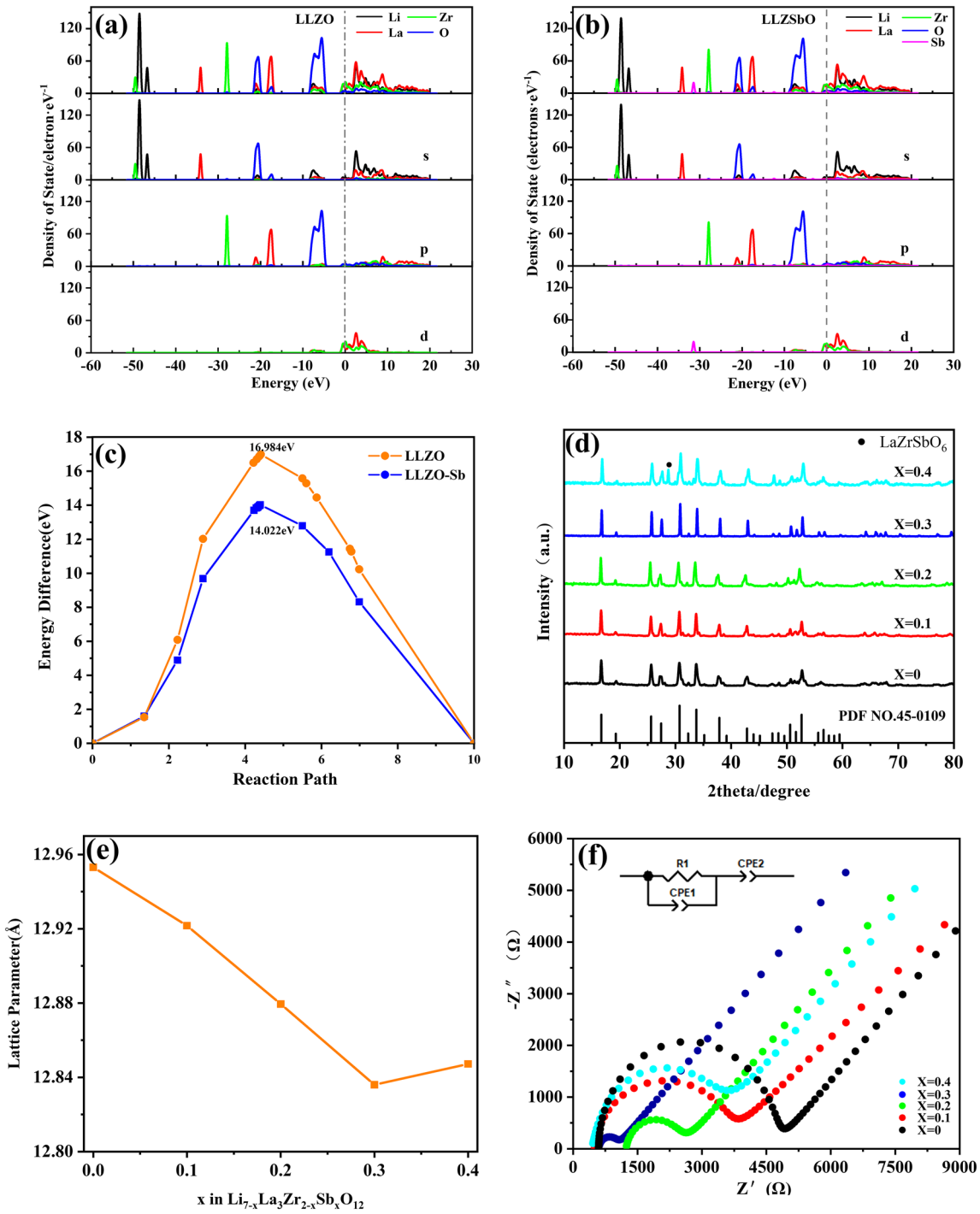

Fig. 2 Theoretical calculation results and experimental characterization of Li7-xLa3Zr2-xSbxO12 (x=0–0.4) electrolyte. **a** LLZO and **b** LLZO-Sb electrolytes elemental partial densities of states. The migration energy barrier with **c** LLZO and LLZO-Sb electrolytes. The electrolytes Li7-xLa3Zr2-xSbxO12 (x=0–0.4) of **d** XRD patterns, **e** the trend curves of lattice parameters with x, f AC impedance plots

transference in the two crystals, and position 1 (0.347176, 0.506243, 0.593238) to position 2 (0.652824, 0.493757, 0.406762) is selected as the research path (Fig. S2). As shown in Fig. 2c, the energy barrier of Li^+ migration in LLZO-Sb is 14.022 eV, which is lower than that of LLZO (16.984 eV). The results explain Sb doped the Zr site of LLZO can improve the conductivity of the electrolyte, which is consistent with the above analysis results.

Table 1 Atomic population values of LLZO and LLZO-Sb

	Orbital and charge	LLZO	LLZSbO
Li	s	2.4	2.07
	Charge	0.6	0.62
O	s	1.84	1.84
	p	5.11	5.12
	Charge	−0.95	−0.96
La	s	2.19	2.19
	p	6.0	6.03
	d	2.07	2.0
	Charge	0.73	0.76
Zr	s	2.31	2.28
	p	6.32	6.63
	d	3.23	3.65
	Charge	0.13	0.14

According to the above theoretical calculation, the synthesis of garnet-type electrolyte was designed reasonably through experiments. To verify LLZO with cubic structure, the XRD of different Sb^{5+} doping levels is shown in Fig. 2d. The diffraction peak of $Li_{7-x}La_3Zr_{2-x}Sb_xO_{12}$ ($x=0$–0.4) is shown in the figure corresponds to the standard peak position of a cubic garnet-like structure (PDF NO.45-0109), indicating that the $Li_{7-x}La_3Zr_{2-x}Sb_xO_{12}$ ($x=0$–0.4) are a pure cubic garnet structure. However, the $Li_{7-x}La_3Zr_{2-x}Sb_xO_{12}$ prepared at $x=0.4$ shows a weak diffraction peak corresponding to the impurity phase $LaZrSbO_6$, indicating that the high content of doping elements is easy to produce impurities [25].

The lattice constant is obtained by refined processing of the XRD data of $Li_{7-x}La_3Zr_{2-x}Sb_xO_{12}$ ($x=0$–0.4) in Fig. 2e. The lattice constant of LLZO ($a=b=c=12.953$) is close to the lattice constant of cubic phase LLZO obtained from the database and the error is only 0.23%, indicating that LLZO is successfully prepared by the solid-state method. The lattice constants of $Li_{7-x}La_3Zr_{2-x}Sb_xO_{12}$ ($x=0.1$–0.4) are all smaller than LLZO. This is because the fact that the Sb^{5+} ion radius (0.61 Å) is smaller than the Zr^{4+} ion radius (0.72 Å) and the replacement of Zr^{4+} by Sb^{5+} causes the crystal volume to become smaller. The decrease in the lattice constant can prove that the element Sb successfully replace the Zr site. However, the lattice constant of the sample composed of $x=0.4$ is higher than that of other components, which may be due to the abnormal increase in lattice constant caused by the $LaZrSbO_6$ impurity phase produced by the high amount of element Sb doping. The similar phenomenon also occurs in the experiment of preparing LLZO by doping with other elements [48, 49].

Figure 2f shows that all the samples ($Li_{7-x}La_3Zr_{2-x}Sb_xO_{12}$ ($x=0$–0.4)) demonstrate the similar Nyquist plots composed of a semi-circular arc and sloping straight line approximately 45°. The intersection of the semi-circular arc and the Z' axis in high frequency range, the diameter of the semi-circular arc and sloping straight in low frequency range represent the grain impedance, the grain boundary resistance and the diffusion process of Li^+ in the electrolyte [50, 51], respectively. As can be seen from Fig. 2f, the grain impedance and grain boundary impedance of $Li_{7-x}La_3Zr_{2-x}Sb_xO_{12}$ prepared by $x=0.2$ is about 1244.5 Ω, 2672.4 Ω, respectively. And the grain impedance of $Li_{7-x}La_3Zr_{2-x}Sb_xO_{12}$ prepared by $x=0.2$ is larger than that of other materials, but the total resistance value of the electrolytes $Li_{7-x}La_3Zr_{2-x}Sb_xO_{12}$ prepared by $x=0.2$ is smaller. The grain impedance of $Li_{7-x}La_3Zr_{2-x}Sb_xO_{12}$ prepared at $x=0.2$ is significantly shifted to low frequency range, which may be caused by the low relative density of the electrolyte resulting in insufficient contact between the grains [50, 51]. As shown in Table S2, the $Li_{7-x}La_3Zr_{2-x}Sb_xO_{12}$ with $x=0.3$ exhibits a highest conductivity of 1.87×10^{-4} S cm^{-1}. Compared with doping with other elements, the ionic conductivity of garnet-type LLZO prepared by the same method is higher than that of other elements [42]. It is shown that Sb can stabilize the cubic phase LLZO and improve its ionic conductivity. When the Sb^{5+} concentration continues to increase to 0.4 the corresponding ion conductivity is dropped. The further increase in Sb^{5+} concentration leads to the decrease in ionic conductivity, which may be attributed to the higher content of heterophase $LaZrSbBO_6$ in the system caused by Sb^{5+} excess. According to the analysis of the above results, when $x=0.3$, $Li_{6.7}La_3Zr_{1.7}Sb_{0.3}O_{12}$ shows the best electrochemical performance. Therefore, $Li_{6.7}La_3Zr_{1.7}Sb_{0.3}O_{12}$ (LLZSbO) was selected as inorganic ceramic fillers for the preparation of CSEs in this experiment.

The prepared LLZO, LLZSbO and CSEs were characterized microscopically by SEM and the elemental surface distribution was tested as shown in Fig. 3. It can be seen that the Sb-doped LLZO particles had good dispersion with particle sizes in the range of 1–3 μm and close alignment between the particles (Fig. 3a, b), indicating that the substitution of Sb^{5+} contributes to the increased denseness of the samples. The surface of CSEs prepared with 20 wt% LLZSbO is shown in Fig. 3c, the CSEs is uniform without voids and has good film-forming property. The cross-section SEM image of CSEs prepared with 20 wt% LLZSbO is displayed in Fig. 3d, the thickness is approximately 105 μm. Moreover, the corresponding EDS elemental mappings indicate that C, O, F, La and Zr elements are homogeneously dispersed in CSEs (Fig. 3e–i), the good distribution of the elements indicates that LLZSbO particles can be uniformly distributed on the PEO matrix without agglomeration, which is beneficial to improve the ionic conductivity of CSEs.

PEO includes crystalline and amorphous areas, while Li^+ mainly relies on the movement of Li^+ in the amorphous zone to realize the migration of Li^+ in the whole process [52]. The impact of LLZSbO ceramic fillers on the crystallinity of the PEO matrix was explored and the XRD of

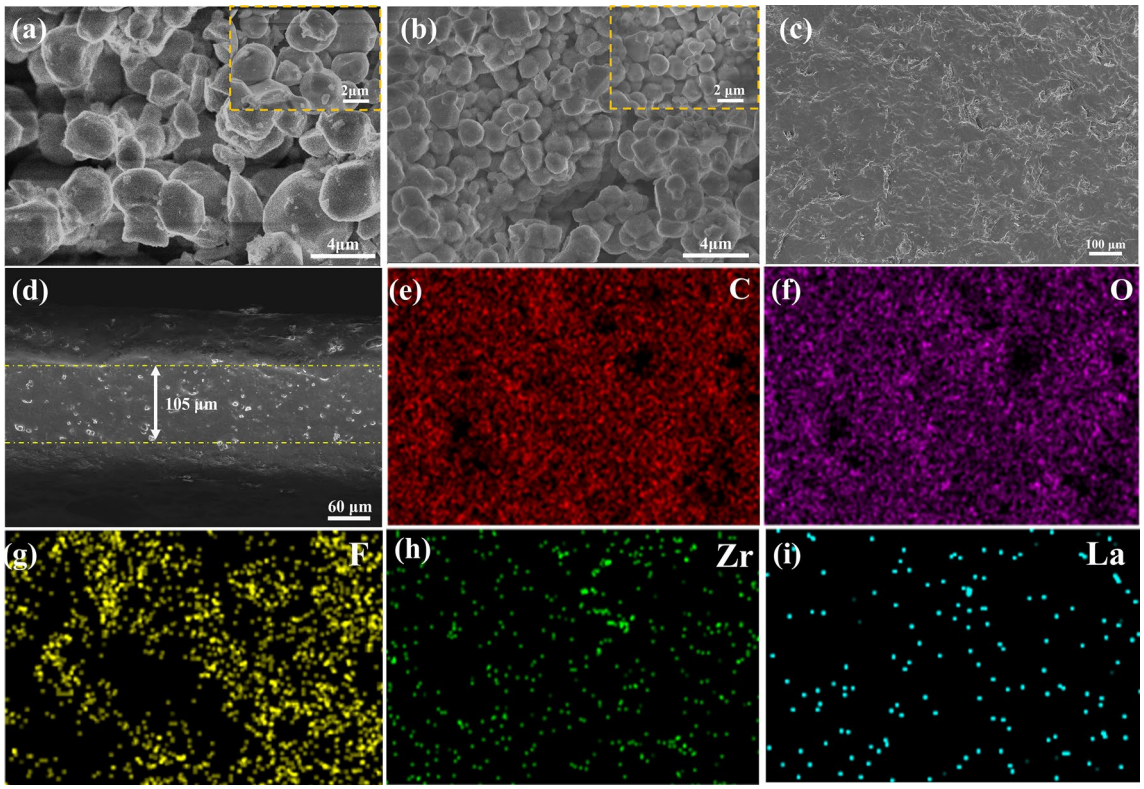

Fig. 3 The surface SEM images of the Li7-xLa3Zr2-xSbxO12 with composition **a** $x=0$ and **b** $x=0.3$, **c** SEM images of CSEs with 20 wt% LLZSbO, **d–i** The cross-section SEM image of CSEs with 20 wt% LLZSbO and the corresponding EDS element mappings of C, O, F, Zr and La

CSEs prepared by adding different amounts of LLZSbO are shown in Fig. 4a. The XRD pattern of the PEO–$LiClO_4$ electrolyte shows two intense diffraction characteristic peaks at $2\theta = 19.1°$ and 23.2°, which indicate that the PEO matrix is in a crystalline state at room temperature. With the increase in LLZSbO concentration, the intensity of diffraction peaks of the PEO matrix gradually reduced, indicating that the addition of LLZSbO could effectively inhibit the crystallization of PEO to increase the amorphous region, which is of great practical significance to improve the lithium-ion migration of CSEs [53].

The effect of LLZSbO concentration on the thermal behavior of the PEO matrix was further determined by DSC, as shown in Fig. 4b. Table S3 shows the thermodynamic

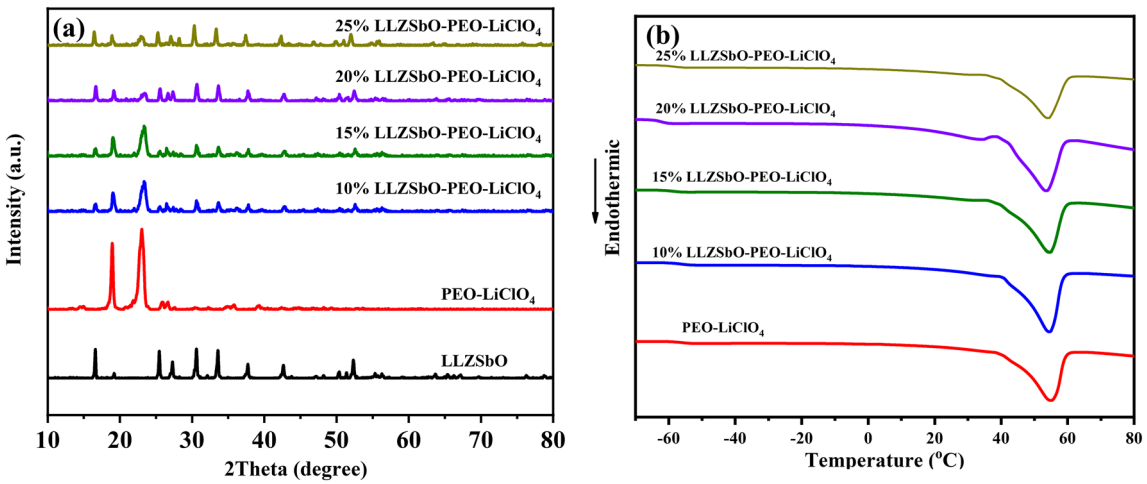

Fig. 4 **a** XRD patterns and **b** DSC curves of the CSEs with various LLZSbO contents

parameters of the tested. It shows that the glass transition temperature (T_g) and the melting temperature (T_m) of PEO-$LiClO_4$ are − 52.84 °C, 54.97 °C, respectively. By adding different concentrations of LLZSbO fillers to the PEO-$LiClO_4$ matrix, the T_g and T_m gradually decrease, indicating that the presence of LLZSbO can effectively destroy the polymer crystallization and enhance the lithium-ion mobility performance [54]. The CSEs prepared with LLZSbO at 20 wt% have the lowest T_m (53.53 °C,), suggesting that the CSEs have a high proportion of amorphous phase internally, which is favorable to ionic transfer at low temperature and improve the ionic conductivity of the CSEs. However, the T_m of CSEs prepared with 25 wt% LLZSbO increase from 53.53 to 54.07 °C, which may be caused by the high LLZSbO content in CSEs. The high concentration of CSEs prepared by LLZSbO leads to internal particle agglomeration, which limits the mobility of lithium ions.

The ionic conductivity of CSEs at room temperature directly affects the practical application of CSEs in ASSLiBs. Figure 5a shows the Arrhenius diagram of CSEs prepared by adding different LLZSbO contents at a temperature of 30–80 °C. Meanwhile, the ionic conductivity of CSEs prepared with different contents of LLZSbO at 30 °C and 60 °C is shown in Table S4. The ionic conductivity of CSEs prepared with 20 wt% LLZSbO is the highest, and the ionic conductivity can reach 0.97×10^{-4} S cm^{-1} and 9.46×10^{-4} S cm^{-1} at 30 °C and 60 °C, respectively, and when compared with CSEs prepared by inorganic fillers Al_2O_3, the ion conductivity has been improved [20]. It shows that LLZSbO prepared by Sb doping has higher ionic conductivity and can be used to prepare CSEs, while the ionic conductivity of PEO-$LiClO_4$ electrolyte at 30 °C and 60 °C is only 6.43×10^{-6} S cm^{-1} and 8.31×10^{-5} S cm^{-1}, respectively. The higher ion conductivity of CSEs prepared with LLZSbO is because the addition of inorganic ceramic fillers promotes the dissolution of lithium salts in CSEs and reduces the crystallinity of PEO, which is consistent with the interpretation of DSC test results. However, when the content of LLZSbO

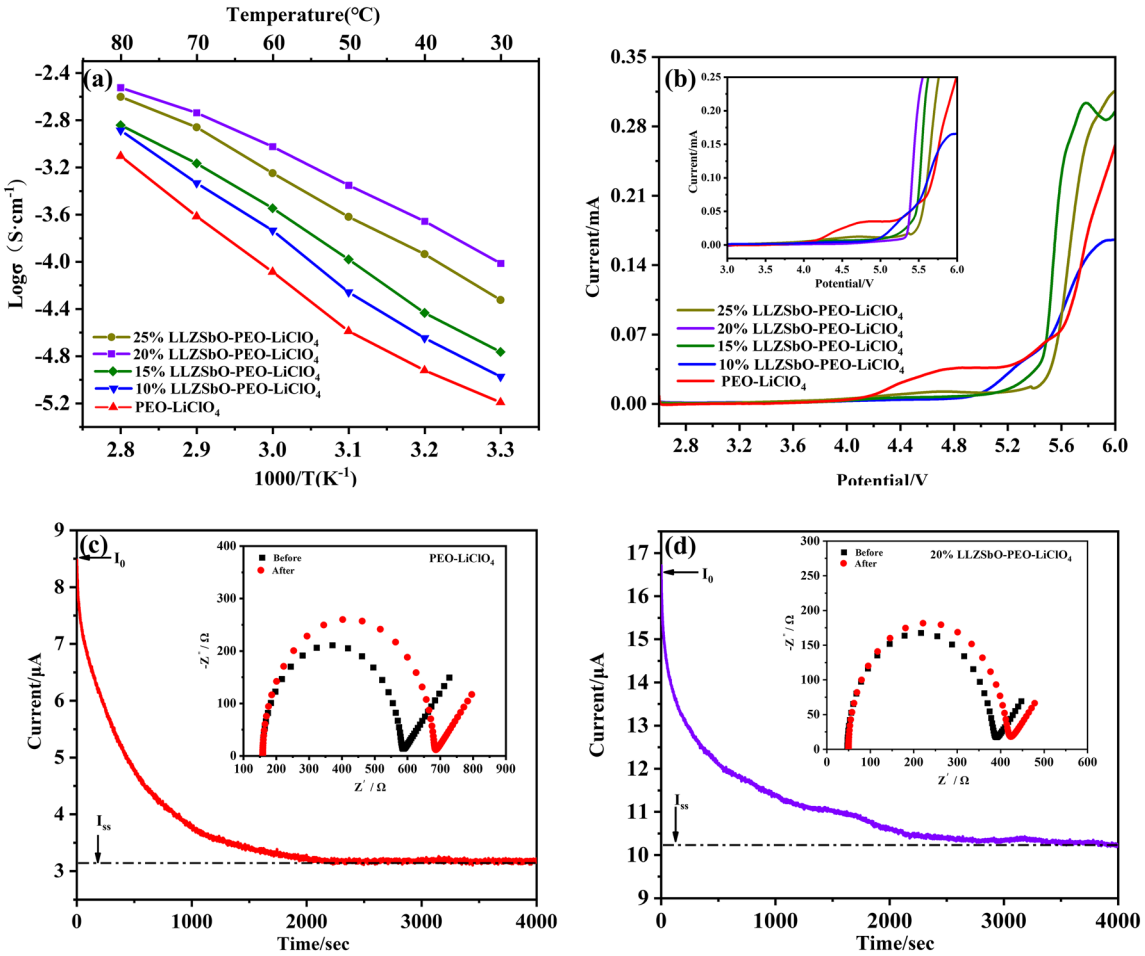

Fig. 5 Electrochemical properties of CSEs. **a** Arrhenius curves of temperature-dependent logσ the CSEs with various LLZSbO contents. **b** LSV curves of the CSEs with various LLZSbO contents at 60 °C. **c–d** The measurement of DC polarization and AC impedance curves for PEO-LiClO4 electrolyte and 20% LLZSbO-PEO-LiClO4 electrolyte at 60 °C

continues to increase, the ionic conductivity of CSEs prepared with LLZSbO decreases, which may be due to the high grain boundary impedance of LLZSbO particles themselves and excessive LLZSbO will increase the impedance of composite polymer electrolyte and lead to the decline of its conductivity.

The electrochemical windows of CSEs with different LLZSbO contents were tested using linear scanning voltammetry (LSV), as shown in Fig. 5b. It can be seen that the PEO-$LiClO_4$ electrolyte has an obvious current reaction when the voltage reaches above 4.2 V, which is mainly due to the oxidation decomposition of the PEO matrix at high potential. However, the electrochemical stability window of CSEs prepared by adding LLZSbO all reaches above 5 V. The electrochemical window of CSEs prepared with 20 wt% LLZSbO is as high as 5.3 V, and there is no obvious current reaction at low potential. The improvement in electrochemical stability of CSEs may be attributed to the good electrochemical stability of LLZSbO (> 5 V) and the strong Lewis acid–base interaction between the acid surface site of LLZSbO [55]. The CSEs prepared with 20 wt% LLZSbO have high electrochemical stability and can be well fitted to the cathodes of high-energy-density batteries.

The solid electrolyte with a high lithium-ion transference number (t^+) can reduce anion movement and inhibit side reactions. The DC polarization and AC impedance were used to test the t^+ of PEO-$LiClO_4$ and CSEs at 60 °C as shown in Fig. 5c, d, and the results are summarized in Table 2. The results show that t^+ of CSEs prepared with 20 wt% LLZSbO was 0.37, much higher than that of PEO-$LiClO_4$ (0.23). This enhancement could be explained by the fact that LLZSbO has a Li^+ transference number close to 1 as well as Li^+ can migrate in both PEO and LLZSbO channels so that the rapid migration of lithium ions in CSEs can be achieved. Consequently, CSEs prepared by adding 20 wt% LLZSbO have a positive effect on improving the migration of Li^+.

Critical current density (CCD) is generally defined as the maximum current density that the solid electrolyte can endure, which is an important parameter for evaluating the inhibition of lithium dendrites [56]. Figure 6a displays the

Table 2 Test parameters and calculation results of lithium-ion transferences number of the PEO-$LiClO_4$ and 20% LLZSbO-PEO-$LiClO_4$ electrolyte

Electrolytes	I_0/μA	Iss/μA	R_0/Ω	Rss/Ω	ΔV/mV	t^+
PEO-$LiClO_4$	8.48	3.15	590.39	688.02	10	0.23
20% LLZSbO-PEO-$LiClO_4$	16.71	10.20	392.57	423.48	10	0.37

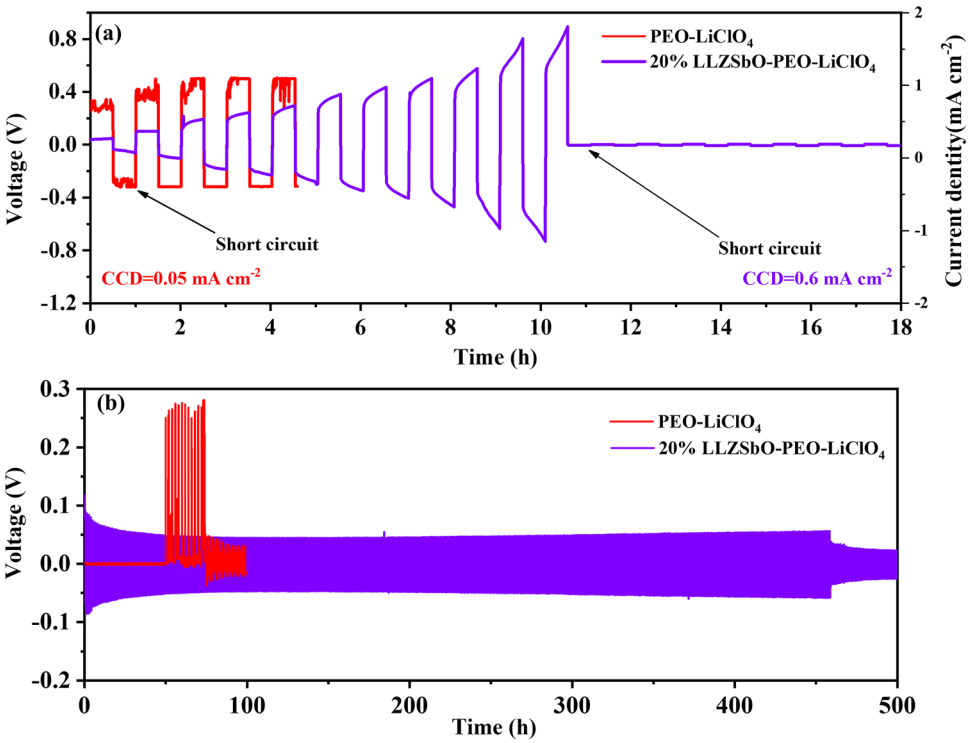

Fig. 6 **a** The CCD of the Li/PEO-LiClO4/Li and Li/20 wt% LLZSbO-PEO-LiClO4/Li cells at 60 °C. **b** Galvanostatic cycling of the Li/PEO-LiClO4/Li and Li/20 wt% LLZSbO-PEO-LiClO4/Li cells at current densities of 0.1 mA·cm^{-2} at 60 °C

CCD of the Li/PEO-$LiClO_4$/Li cell is only 0.05 mA cm^{-2} due to the poor interface, while the CCD of the Li/20% LLZSbO-PEO-$LiClO_4$/Li cell is substantially improved to 0.6 mA cm^{-2}. In order to further study the interface compatible between the electrolyte and metal lithium electrodes, the galvanostatic cycling performance tests of PEO-$LiClO_4$ and 20% LLZSbO-PEO-$LiClO_4$ were performed at 0.1 mA cm^{-2} and 60 °C, as shown in Fig. 6b. The voltage of the PEO-$LiClO_4$ polymer electrolyte is unstable, and a short circuit exists during the stripping and plating process in Fig. 6b, and this may be due to the side reaction that occurs between PEO-$LiClO_4$ and Li metal, which leads to the lithium dendrites are pierced. However, it shows the symmetric cell assembled by CSEs prepared with 20 wt% LLZSbO gradually stabilizes the voltage at 0.024 V during galvanostatic cycling and can continue to cycle steadily over 500 h without a short circuit. Meanwhile, as the galvanostatic cycling exceeds 450 h, the voltage gradually decreases, possibly owing to the improvement in the interface between the CSEs and the lithium metal during the striping and plating process [54]. It indicates that the addition of LLZSbO to prepare CSEs has better mechanical properties, which can hinder the side reaction between PEO and metal Li anode to restrain the growth of lithium dendrite.

In order to study the electrochemical performance of as-prepared material, we have carried out a comparative experiment by using PEO-$LiClO_4$ electrolyte and CSEs with 20 wt% LLZSbO to assemble a full battery for electrochemical testing, respectively. Figure 7a and Figure S3 show that the charge and discharge voltage profiles of the LFP/20% LLZSbO-PEO-$LiClO_4$/Li and LFP/PEO-$LiClO_4$/Li cells with various rates from 0.1 to 1 C at 60 °C. The cell with CSEs prepared with 20 wt% of LLZSbO has a smaller voltage platform gap than that with PEO-$LiClO_4$, which is attributed to the high ionic conductivity of CSEs in LFP/20% LLZSbO-PEO-$LiClO_4$/Li and the excellent

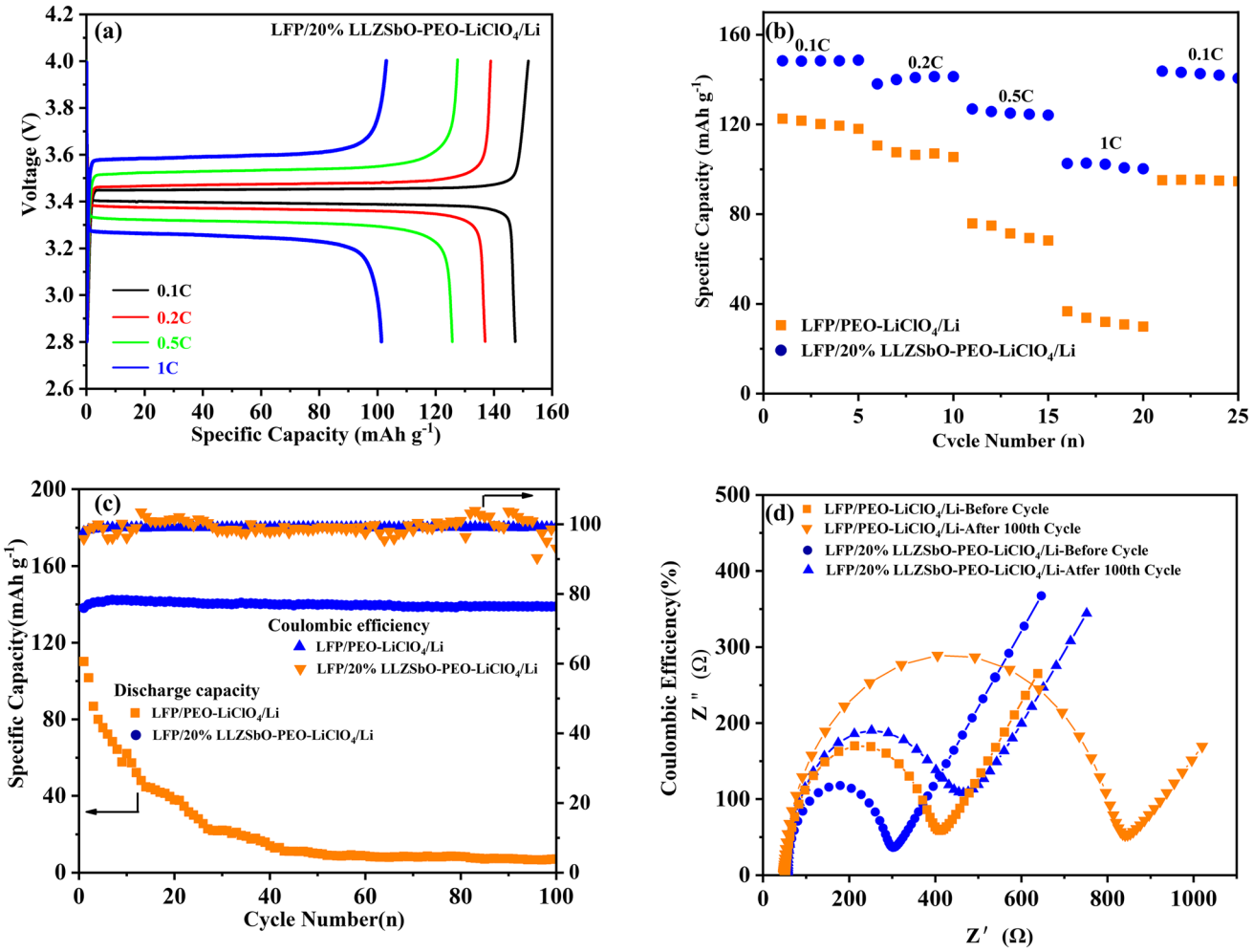

Fig. 7 Electrochemical performance of LFP/20% LLZSbO-PEO-LiClO4/Li and LFP/PEO-LiClO4/Li cells at 60 °C. **a** Charge and discharge voltage profiles at different rates. **b** Rate performance at 0.1–1 C. **c** Cycling performance and columbic efficiency at 0.2 C. **d** AC impedance diagrams before cycles and after 100 cycles

interface stability between the CSEs and the metal Li anode. Figure 7b shows that the rate performance of the LFP/20% LLZSbO-PEO-$LiClO_4$/Li cell is 148.4 mAh g^{-1}, 138.1 mAh g^{-1}, 126.9 mAh g^{-1}, 102.6 mAh g^{-1} from 0.1 to 1 C, respectively. However, the capacity of the LFP/PEO-$LiClO_4$/Li battery is only 122.5 mAh g^{-1} at 0.1 C. When the rate increases to 0.5C, the specific capacity of the battery begins to decrease significantly to 75.8 mAh g^{-1}, which indicates that the PEO-$LiClO_4$ electrolyte is difficult to meet the charge and discharge behavior of the battery at high rates. Figure 7c shows the cycling performance curves of two batteries at 0.2 C, and it can be seen that the discharge specific capacity of the LFP/20% LLZSbO-PEO-$LiClO_4$/Li cell increases during the initial five cycles because of the adjustment of the interface between the metal lithium anode and the CSEs. During this process, the CSEs and the electrode will gradually open and form a stable Li^+ channel [16]. After five cycles, the discharge specific capacity increases from 138.1 mAh g^{-1} to 142.3 mAh g^{-1}. Meanwhile, the capacity retention of LFP/20% LLZSbO-PEO-$LiClO_4$/Li cell is 97.5%, while the capacity retention of PEO-$LiClO_4$ electrolyte is only 6.4% after 100 cycles. This indicates that the CSEs prepared by adding LLZSbO to PEO-$LiClO_4$ have excellent cycling stability for ASSLiBs. Figure 7d shows the AC impedance spectra of the two cells before and after 100 cycles at 0.2 C. The impedances of before and after the cycle the LFP/20% LLZSbO-PEO-$LiClO_4$/Li cell are 301.4 Ω and 465.5 Ω, while the LFP/PEO-$LiClO_4$/Li cell's impedance are 414.3 Ω and 846.5 Ω, respectively. Compared with the LFP/PEO-$LiClO_4$/Li cell, the average increasing impedance per cycle of the cell with CSEs prepared with 20 wt% LLZSbO is less than 2 Ω, indicating that the CSEs and the electrode interface maintain good contact during the cycles. Based on the above analysis, the excellent cycle and rate performance of the LFP/20% LLZSbO-PEO-$LiClO_4$/Li battery indicate that CSEs with 20 wt% LLZSbO is feasible to be used in ASSLiBs.

4 Conclusion

In summary, we have reported the electronic structure and ion migration of garnet-type LLZO and Sb-doped LLZO electrolytes were studied by the first-principles method based on DFT. It indicates that the structure of the Sb-doped LLZO is stable and more favorable for improving ionic migration. On the basis of theoretical calculations and experiments, CSEs prepared by adding $Li_{6.7}La_3Zr_{1.7}Sb_{0.3}O_{12}$ (LLZSbO) to the PEO-$LiClO_4$ matrix can reach 0.97×10^{-4} S cm^{-1} at 30 °C with a wider electrochemical window of 5.3 V. The thermal behavior of CSEs was characterized by DSC, which shows that adding 20 wt% LLZSbO to the PEO-$LiClO_4$ matrix can effectively increase the proportion of the amorphous phase of CSEs. The CSEs prepared with a concentration of 20 wt% LLZSbO to has a high lithium ion transference number of 0.37. The results of the Li/20% LLZSbO-PEO-$LiClO_4$/Li cell can cycle stably for nearly 500 h at a current density of 0.1 mA cm^{-2}. Moreover, the ASSLiBs assembled with CSEs prepared with 20% LLZSbO delivers a high initial discharge capacity of 148.4 mAh g^{-1} at 0.1 C and has relatively stable specific capacity of 138.8 mAh g^{-1} even after 100 cycles at 0.2 C. Therefore, the design of solid-state electrolyte according to the first-principles calculation is applied to the all-solid-state battery, which can provide theoretical support for the improvement of the electrochemical performance of the all-solid-state battery.

Supplementary Information The online version contains supplementary material available at https://doi.org/10.1007/s00339-021-05128-x.

Acknowledgements This research was supported by the National Natural Science Foundation of China (No.52161033), Guangxi Natural Science Foundation (No. 2020GXNSFAA297082), (2019GXNSFBA245099) and (2020GXNSFAA297019), the Fund Project of the GDAS Special Project of Science and Technology Development, Guangdong Academy of Sciences Program (No.2020GDASYL-20200104030), the Innovation Project of Guangxi University of Science and Technology Graduate Education (YCSW2021324), Guangxi Innovation Driven Development Project (No.AA18242036-2), and the Fund Project of the Key Lab of Guangdong for Modern Surface EngineeringTechnology(No. 2018KFKT01) and supported by the Guangxi Key Laboratory of Low Carbon Energy Material (2020GKLLCEM01).

Funding Guangxi natural science foundation, 2019GXNSFBA245099 funded by Guanhua Yang

Declarations

Conflict of interest The authors declare that they have no competing interests.

References

1. M. Armand, J.M. Tarascon, Nature **451**, 652 (2008)
2. A. Manthiram, ACS Cent. Sci. **3**, 1063 (2017)
3. R.S. Chen, Q.H. Li, X.Q. Yu, L.Q. Chen, H. Li, Chem. Rev. **120**, 6820 (2020)
4. J.G. Kim, B. Son, S. Mukherjee, N. Schuppert, A. Bates, O. Kwon, M.J. Choi, H.Y. Chung, S. Park, J. Power Sources **282**, 299 (2015)
5. J. Chen, J.W. Wu, X.D. Wang, A.A. Zhou, Z.L. Yang, Energy Storage Mater. **35**, 70 (2021)
6. C. Sun, J. Liu, Y. Gong, D.P. Wilkinson, J. Zhang, Nano Energy **33**, 363 (2017)
7. N. Nitta, F.X. Wu, J.T. Lee, G. Yushin, Mater. Today **18**, 252 (2015)
8. G.Q. Tan, F. Wu, C. Zhan, J. Wang, D.B. Mu, J. Lu, K. Amine, Nano Lett. **16**, 1960 (2016)
9. W.W. Wang, Z.Q. Fang, M. Zhao, Y. Peng, J.J. Zhang, S.Y. Guan, Chem. Phys. Lett. **747**, 137335 (2020)

10. Z.G. Xue, D. He, X.L. Xie, J. Mater. Chem. A **3**, 19218 (2015)
11. J.X. Zhang, N. Zhao, M. Zhang, Y.Q. Li, P.K. Chu, X.X. Guo, Z.F. Di, X. Wang, H. Li, Nano Energy **28**, 447 (2016)
12. Y.H. Zhang, F. Chen, D.J. Yang, W.P. Zha, J.Y. Li, Q. Shen, X.L. Zhang, L.M. Zhang, J. Electrochem. Soc. **164**, 1695 (2017)
13. X.W. Huang, S.Y. Liao, Y.D. Liu, Q.S. Rao, X.K. Peng, Y.G. Min, Electrochim. Acta **389**, 0013 (2021)
14. K.C.C. Sun, A. Yusuf, S.W. Li, X.L. Qi, Y. Ma, D.Y. Wang, Chem. Eng. J. **414**, 1385 (2021)
15. F. Wu, Z.Y. Wen, Z.K. Zhao, J.Y. Bi, Y.X. Shang, Y.H. Liang, L. Li, N. Chen, Y.J. Li, R.J. Chen, Energy Storage Mater. **38**, 447 (2021)
16. B. Chen, Z. Huang, X.T. Chen, Y.R. Zhao, Q. Xu, P. Long, S.J. Chen, X.X. Xu, Electrochim. Acta **210**, 905 (2016)
17. S.J. Tan, X.X. Zeng, Q. Ma, X.W. Wu, Y.G. Guo, Electrochem. Energy Rev. **1**, 113 (2018)
18. Z.W. Cheng, T. Liu, B. Zhao, F. Shen, H.Y. Jin, X.G. Han, Energy Storage Mater. **34**, 388 (2021)
19. H.W. Zhai, P.Y. Xu, M.Q. Ning, Q. Cheng, J. Mandal, Y. Yang, Nano Lett. **17**, 318 (2017)
20. K.K. Wimalaweera, V.A. Seneviratne, M.A.K.L. Dissanayake, Proced. Eng. **215**, 109 (2017)
21. Y.C. Jung, S.M. Lee, J.H. Choi, S.S. Jang, D.W. Kim, Electrochem. Soc. **162**, 704 (2015)
22. W. Liu, N. Liu, J. Sun, P.C. Hsu, Y.Z. Li, H.W. Lee, Y. Cui, Nano lett. **15**, 2740 (2015)
23. R.-G. Li, S.-T. Guo, L. Yu, L.-B. Wang, D.-B. Wu, Y.-Q. Li, X.-L. Hu, Adv. Mater Interfaces **6**, 1900200 (2019)
24. M.M. Raju, F. Altayran, M. Johnson, D.L. Wang, Q.F. Zhang, Electrochem **2**, 390 (2021)
25. L.B. Zhuang, X. Huang, Y. Lu, J.W. Tang, Y.J. Zhou, X. Ao, Y. Yang, B.B. Tian, Ceram. Int. **47**, 22768 (2021)
26. Z.Z. Cao, Y. Li, J.Y. Su, J.J. Zhao, Y. Li, S. Yan, Q. Liu, T.F. He, H. Zhang, G.R. Li, Ionics **27**, 1861 (2021)
27. X. Xiang, F. Chen, W.Y. Yang, J.B. Yang, X.B. Ma, D.F. Chen, K. Su, Q. Shen, L.M. Zhang, J. Am. Ceram. Soc. **103**, 2483 (2020)
28. D. Rettenwander, P. Blaha, Q. Laskowski, K. Schwarz, P. Bottke, L. Wilkening, C.A. Geiger, G. Amthauer, Chem. Mater. **26**(8), 2617 (2014)
29. D. Rettenwander, J. Langer, W. Schmidt, C. Arrer, K.J. Harris, V. Terskikh, G.R. Goward, M. Wilkening, G. Amthauer, Chem. Mater. **27**(8), 3135 (2015)
30. S. Ramakumar, L. Satyanarayana, S.V. Manorama, R. Murugan, Phys. Chem. Chem. Phys. **15**(27), 11327 (2013)
31. T. Yang, Y. Li, W. Wu, Z. Cao, W. He, Y. Gao, J. Liu, G. Li, Ceram. Int. **44**(2), 1538 (2018)
32. T.H. Wan, Z.H. Lu, F. Ciucci, J. Power Sources **390**, 61 (2018)
33. B. Andriyevsky, K. Doll, T. Jacob, Mater. Chem. Phys. **185**, 210 (2017)
34. S. Kc, R.C. Longo, K. Xiong, K. Cho, Solid State Ion. **261**, 100 (2014)
35. L.J. Miara, S.P. Ong, Y. Mo, W.D. Richards, Y. Park, J.M. Lee, H.S. Lee, G. Ceder, Chem. Mater. **25**, 3048 (2013)
36. T. Yang, J. Zheng, Q. Cheng, Y.Y. Hu, C.K. Chan, A.C.S. Appl, Mater. Inter. **9**(26), 21773 (2017)
37. Z. Li, H.M. Huang, J.K. Zhu, J.F. Wu, H. Yang, L. Wei, X. Guo, A.C.S. Appl, Mater. Inter. **11**(1), 784 (2019)
38. X. Ma, Y. Xu, B. Zhang, X. Xue, C. Wang, S. He, J. Lin, L. Yang, J. Power Sources **453**, 227881 (2020)
39. S.H.S. Cheng, K.Q. He, Y. Liu, J.W. Zha, M. Kamruzzaman, R.L.W. Ma, Z.M. Dang, R.K.Y. Li, C.Y. Chung, Electrochim. Acta **253**, 430 (2017)
40. S.F. Song, Y.M. Wu, W.P. Tang, F. Deng, J.Y. Yao, Z.W. Liu, R.J. Hu, ZY Wen. Alamusi, L. Lu, N. Hu, ACS Sustain. Chem. Eng. **7**, 713 (2019)
41. J.P. Perdew, K. Burke, M. Ernzerhof, Phys. Rev. Lett. **77**, 3865 (1996)
42. E. Hanc, W. Zając, J. Molenda, Solid State Ionics **262**, 617 (2014)
43. Y. Hu, X. Zhu, H. Zou, L. Zheng, S. Song, Z. Song, J. Alloy. Compd. **696**, 150 (2017)
44. Y. Li, Z. Wang, Y. Cao, F. Du, C. Chen, Z. Cui, X. Guo, Electrochim. Acta **180**, 37 (2015)
45. W.F. Egelhoff, Surf. Sci. Rep. **6**, 253 (1987)
46. A. Kızılaslan, M. Kırkbınar, T. Cetinkaya, H. Akbulut, Phys. Chem. Chem. Phys. **22**, 17221 (2020)
47. Y.H. Li, Z.J. Sun, D.Y. Liu, Y.Y. Gao, Y.K. Wang, H.T. Bu, M.T. Li, Y.F. Zhang, G.X. Gao, S.J. Ding, J. Mater. Chem. A **8**, 2021 (2020)
48. Z.L. Hu, H.D. Liu, H.B. Ruan, R. Hu, Y.Y. Su, L. Zhang, Ceram. Int. **42**, 12156 (2016)
49. T.T. Yang, Y. Li, W.W. Wu, Z.Z. Cao, W.Y. He, T.F. Gao, J.R. Liu, G.R. Li, Ceram. Int. **44**, 1538 (2018)
50. W. Choi, H.C. Shin, J.M. Kim, J.Y. Choi, W.-S. Yoon, J. Electrochem. Sci. Te. **11**(1), 1 (2020)
51. C. Shao, Z. Yu, H. Liu, Z. Zheng, N. Sun, C. Diao, Electrochim. Acta **225**, 345 (2017)
52. E.C. Self, Z.D. Hood, T. Brahmbhatt, F.M. Delnick, H.M. Meyer, G. Yang, J.L.M. Rupp, J. Nanda, Chem. Mater. **32**, 8789 (2020)
53. Z. Sun, Y. Li, S. Zhang, L. Shi, H. Wu, H. Bu, S. Ding, J. Mater. Chem. A **7**, 11069 (2019)
54. Z. Wan, D. Lei, W. Yang, C. Liu, K. Shi, X. Hao, L. Shen, W. Lv, B. Li, Q.H. Yang, F. Kang, Y.B. He, Adv. Funct. Mater. **29**, 1970006 (2019)
55. C. Liu, J.X. Wang, W.J. Kou, Z.H. Yang, P.F. Zhai, Y. Liu, W.J. Wu, J.T. Wang, Chem. Eng. J. **404**, 1385 (2021)
56. Y. Lu, C.Z. Zhao, H. Yuan, X.B. Cheng, J.Q. Huang, Q. Zhang, Adv. Funct. Mater. **31**(18), 2009925 (2021)